

Unusual Physical and Chemical Properties of Cu in $\text{Ce}_{1-x}\text{Cu}_x\text{O}_2$ Oxides

Xianqin Wang,[†] José A. Rodríguez,^{*,‡} Jonathan C. Hanson,[†] Daniel Gamarra,[‡] Arturo Martínez-Arias,^{*,‡} and Marcos Fernández-García^{*,‡}

Chemistry Department, Brookhaven National Laboratory, Upton, New York 11973, and Instituto de Catálisis y Petroleoquímica, CSIC, Campus Cantoblanco, 28049 Madrid, Spain

Received: April 15, 2005; In Final Form: August 9, 2005

The structural and electronic properties of $\text{Ce}_{1-x}\text{Cu}_x\text{O}_2$ nano systems prepared by a reverse microemulsion method were characterized with synchrotron-based X-ray diffraction, X-ray absorption spectroscopy, Raman spectroscopy, and density functional calculations. The Cu atoms embedded in ceria had an oxidation state higher than those of the cations in Cu_2O or CuO . The lattice of the $\text{Ce}_{1-x}\text{Cu}_x\text{O}_2$ systems still adopted a fluorite-type structure, but it was highly distorted with multiple cation–oxygen distances with respect to the single cation–oxygen bond distance seen in pure ceria. The doping of CeO_2 with copper introduced a large strain into the oxide lattice and favored the formation of O vacancies, leading to a $\text{Ce}_{1-x}\text{Cu}_x\text{O}_{2-y}$ stoichiometry for our materials. Cu approached the planar geometry characteristic of Cu(II) oxides, but with a strongly perturbed local order. The chemical activities of the $\text{Ce}_{1-x}\text{Cu}_x\text{O}_2$ nanoparticles were tested using the reactions with H_2 and O_2 as probes. During the reduction in hydrogen, an induction time was observed and became shorter after raising the reaction temperature. The fraction of copper that could be reduced in the $\text{Ce}_{1-x}\text{Cu}_x\text{O}_2$ oxides also depended strongly on the reaction temperature. A comparison with data for the reduction of pure copper oxides indicated that the copper embedded in ceria was much more difficult to reduce. The reduction of the $\text{Ce}_{1-x}\text{Cu}_x\text{O}_2$ nanoparticles was rather reversible, without the generation of a significant amount of CuO or Cu_2O phases during reoxidation. This reversible process demonstrates the unusual structural and chemical properties of the Cu-doped ceria materials.

Introduction

CuO – CeO_2 mixed-metal oxides have important applications as electrolytes in fuel cells,^{1,2} gas sensors,³ and efficient catalysts for various reactions such as the combustion of CO and methane,^{4–7} the water-gas shift reaction,^{7–9} the reduction of SO_2 by CO,¹⁰ methanol synthesis,¹¹ and the wet oxidation of phenol.¹² A recent study has even reported that Cu/CeO_2 catalysts exhibited superior activity when compared to the industrial Cu/ZnO catalysts for the steam-reforming methanol reaction.^{13,14} Furthermore, copper oxide-based catalysts have been considered as suitable substitutes for noble metal catalysts in emission control applications for novel, clean fuels due to their high activities and lower cost.^{13–15} It is anticipated that, with proper development, metal-promoted ceria catalysts should realize much higher CO conversions than commercial Cu/ZnO catalysts.^{9,13–15}

In this study, we investigate the behavior of nanoparticles of $\text{Ce}_{1-x}\text{Cu}_x\text{O}_2$ solid solutions prepared following a novel procedure.^{5,16,17} Since the dopant is incorporated into a fluorite-type crystal structure that is very different from the structures of CuO or Cu_2O (see Figure 1), it is not clear what to expect for the physical and chemical properties of $\text{Ce}_{1-x}\text{Cu}_x\text{O}_2$. In principle, a Cu cation embedded in a fluorite lattice can have up to eight oxygen neighbors versus four in CuO and two in Cu_2O . Moreover, Cu does not adopt formal oxidation states of “+4” and “+3” like Ce does. These differences open the possibility for substantial structural perturbations (stress, point, and line defects, O vacancies)¹⁸ within the ceria lattice.

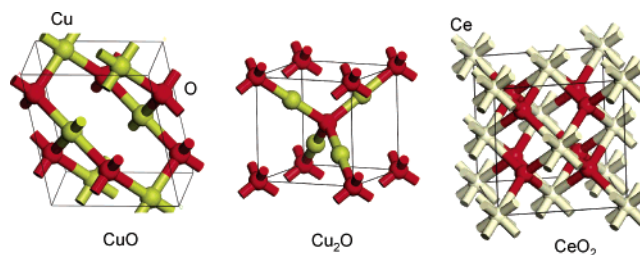


Figure 1. Crystal structures of CuO , Cu_2O , and CeO_2 .

Previous work indicates that Cu-doped ceria has better redox properties and oxygen storage capacity than those of pure ceria.⁷ The combination of the redox properties and oxygen storage capacity of ceria as well as the interaction between ceria and Cu are usually claimed for the significant activities of CuO – CeO_2 catalysts.^{7c,9,19,20,21} To address these issues, a series of $\text{Ce}_{1-x}\text{Cu}_x\text{O}_2$ and $\text{CuO}_x/\text{CeO}_2$ samples were prepared in this work. Their structural and electronic properties were investigated employing X-ray diffraction (XRD), X-ray absorption fine structure (XAFS), Raman spectroscopy, and density functional (DF) calculations. Since CuO – CeO_2 catalysts interact with hydrogen in many reaction processes,^{7–15} we studied the reduction in H_2 of the $\text{Ce}_{1-x}\text{Cu}_x\text{O}_2$ and $\text{CuO}_x/\text{CeO}_2$ systems using synchrotron-based in-situ time-resolved XRD and XAFS. Recently, these techniques were successfully used to study the kinetics and mechanism for the reduction of CuO and Cu_2O .^{22,23} They showed a direct transformation pathway for CuO reduction ($\text{CuO} \rightarrow \text{Cu}$) when there was a large supply of H_2 , while a sequential reduction pathway involving one intermediate ($\text{CuO} \rightarrow \text{Cu}_2\text{O} \rightarrow \text{Cu}$) was observed when there was a limited supply

* Corresponding authors.

[†] Brookhaven National Laboratory.

[‡] Instituto de Catálisis y Petroleoquímica, CSIC.

of H_2 . During the reduction of CuO , the oxide system can reach metastable states (MS) and react with hydrogen instead of forming Cu_2O . To see the formation of Cu_2O , one has to limit the flow of hydrogen, slowing the rate of reduction to allow a $\text{MS} \rightarrow \text{Cu}_2\text{O}$ transformation.²² Our results of time-resolved XRD and XAFS show important differences in the kinetics for the reduction of CuO and $\text{Ce}_{1-x}\text{Cu}_x\text{O}_2$. This may be a consequence of the unusual structural and electronic properties for the Cu atoms embedded in ceria.

Experimental and Theoretical Methods

Sample Preparation. The reference CuO , Cu_2O , and Cu bulk samples used in this work were obtained from commercial sources (>99.99% purity). Cu-doped ceria, labeled as $\text{Ce}_{1-x}\text{Cu}_x\text{O}_2$ ($x = 0.05, 0.1$, and 0.2) was prepared with a modified reverse microemulsion method.^{5,16,17} Briefly, the precursors were introduced in a reverse microemulsion (water in oil) using *n*-heptane as the organic phase, Triton X-100 (Aldrich) as surfactant, and hexanol as cosurfactant. Then, this suspension was mixed with another similar suspension containing an aqueous phase in alkali solution (TMAH, Aldrich). All cations were coprecipitated, and the resulting mixtures were stirred for 24 h, centrifuged, decanted, and rinsed with methanol. Finally, the solid portion was dried overnight at 100 °C, and the resulting powders were calcined under air at 500 °C for 2 h. ICP-AES chemical analysis of these samples confirmed quantitative precipitation of both Cu and Ce cations. Surface area values (S_{BET})^{5,7} obtained for these samples were observed to increase with the copper content (130, 136, and 151 $\text{m}^2 \text{g}^{-1}$ for $\text{Ce}_{0.95}\text{Cu}_{0.05}\text{O}_2$, $\text{Ce}_{0.9}\text{Cu}_{0.1}\text{O}_2$ and $\text{Ce}_{0.8}\text{Cu}_{0.2}\text{O}_2$, respectively), in agreement with the gradual particle size decrease (as shown below). It is interesting that this contrasts with results by Shan et al.^{7f} which report a decrease of S_{BET} with increasing copper content in Ce–Cu mixed oxide samples prepared by complexation–combustion.

Two samples of copper supported on CeO_2 (Cu wt % of 3 and 5, denoted hereafter as 3Cu and 5Cu, respectively) were prepared by incipient wetness impregnation of a CeO_2 support prepared by microemulsion (in a similar manner as described above) with copper nitrate aqueous solutions. Following impregnation, the samples were dried overnight at 100 °C and finally were calcined under air at 500 °C for 2 h. S_{BET} values obtained for these samples prepared by impregnation were of 106 and 101 $\text{m}^2 \text{g}^{-1}$ for 3Cu and 5Cu, respectively, close to that of the parent CeO_2 support.

Time-Resolved XRD. The time-resolved X-ray diffraction experiments were carried out on beamlines X7B ($\lambda = 0.922 \text{ \AA}$, $Q \leq 6 \text{ \AA}^{-1}$) and X17B1 ($\lambda = 0.165 \text{ \AA}$, $Q \leq 15 \text{ \AA}^{-1}$) of the National Synchrotron Light Source (NSLS) at Brookhaven National Laboratory. The sample was loaded into a sapphire capillary cell which was attached to a flow system.^{23,24} A small resistance heater was wrapped around the capillary, and the temperature was monitored with a 0.1-mm chromel–alumel thermocouple that was placed in the capillary near the sample. A MAR345 detector was used to record X-ray patterns. Two-dimensional powder patterns were collected with a Mar345 image plate detector, and the powder rings were integrated using the FIT2D code.²⁵ In-situ diffraction patterns were collected during reduction and reoxidation. These reactions were carried out isothermally at different temperatures (180, 200, 300, and 400 °C) with a 5% H_2 and 95% He gas mixture for the reduction and a 5% O_2 and 95% He gas mixture for the reoxidation at a flow rate of ~20 mL/min.

Raman. Raman spectra were collected at room temperature using a Renishaw Dispersive System 1000 equipped with a

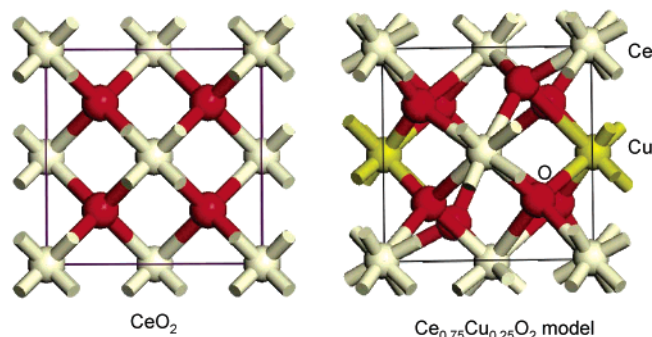
cooled CCD detector and holographic Notch filter. The samples were excited with the red laser line (632.8 nm); the spectral resolution was $\sim 3 \text{ cm}^{-1}$, and the spectrum acquisition consisted of two accumulations with a total of ~ 10 min acquisition time.

XAFS. Cu K absorption edge XAFS spectra were collected in air at room temperature and in-situ during the reduction of the catalysts in a flow of a 5% H_2 and 95% He gas mixture ($\sim 20 \text{ mL/min}$) at beamline X18B of the NSLS at BNL. A commercially available Lytle cell was used for mounting the sample.²⁶ First, the sample was brushed on an adhesive Kapton tape. Next, the stripe of Kapton tape was loaded into the same cell used for in-situ XRD and heated to the desired temperature. The X-ray absorption spectra were taken repeatedly in the “fluorescence-yield mode” using a pips (passivated-implanted planar silicon) detector cooled with circulating water. The monochromator was detuned 15% in order to reduce the amount of higher harmonics in the beam. The spectra were scanned in the range of 8700–9900 eV for the Cu K-edge.²⁷ The photon energy was calibrated for each scan with the first inflection point of the Cu K-edge in Cu metal foil. Both the incident (I_0) and transmitted (I) synchrotron beam intensities were measured simultaneously using an ionization chamber filled with 100% N_2 gas and a mixture of 50% Ar and 50% N_2 , respectively. EXAFS data have been analyzed using the Athena and Artemis programs.²⁸ They allow background removal by optimization of the low- R portion of the EXAFS data (i.e., minimizing the average value of the low- R Fourier transform, maintaining at the same time the value for the first coordination shell at maximum).²⁹

DF Calculations. The first-principles DF calculations reported in section III were performed using the CASTEP (Cambridge Serial Total Energy Package) suite of programs.³⁰ CASTEP has an excellent track record in accurate prediction of geometry and energetics for oxide systems.^{30a,31–34} In this code, the wave functions of valence electrons are expanded in a plane wave basis set with k -vectors within a specified energy cutoff E_{cut} . Tightly bound core electrons are represented by nonlocal ultrasoft pseudopotentials.³⁵ Brillouin Zone integration is approximated by a sum over special k -points chosen using the Monkhorst-Pack scheme.³⁶ In all the calculations, the kinetic energy cutoff E_{cut} (400 eV) and the density of the Monkhorst-Pack k -point mesh were chosen high enough in order to ensure convergence of the computed structures and energetics. The exchange-correlation contribution to the total electronic energy was treated in a generalized-gradient-corrected (GGA) form of the local density approximation (LDA): Perdew–Burke–Ernzerhoff functional.³⁷ The structural parameters of the bulk CeO_2 and $\text{Ce}_{1-x}\text{Cu}_x\text{O}_2$ systems in their different configurations were determined using the Broyden–Fletcher–Goldfarb–Shanno (BFGS) minimization technique, with the following thresholds for the converged structures: energy change per atom less than $5 \times 10^{-6} \text{ eV}$, residual force less than 0.02 eV/C, the displacement of atoms during the geometry optimization less than 0.001 C, and the rms of the stress tensor less than 0.1 GPa. For each optimized structure, the partial charges on the atoms were estimated by projecting the occupied one-electron eigenstates onto a localized basis set (which included pseudo-orbitals representing the valence levels of O, Ce, and Cu) with a subsequent Mulliken population analysis.³⁸ Any charge partition scheme has approximations,³⁹ but the Mulliken analysis has been shown frequently to be useful for studying qualitative trends in charge distribution.^{32,38a,39} The Mulliken analysis is used in many studies and can provide qualitative trends similar to those obtained with more sophisticated schemes for charge partition

TABLE 1: Calculated Lattice Constants for Copper Oxides and Ceria

compound	cell dimensions	
	DF calcd	expt
CuO(C2/c)	$a = 4.628 \text{ \AA}$	$a = 4.653 \text{ \AA}^a$
	$b = 3.548 \text{ \AA}$	$b = 3.410 \text{ \AA}$
	$c = 5.154 \text{ \AA}$	$c = 5.108 \text{ \AA}$
	$\beta = 99.52^\circ$	$\beta = 99.50^\circ$
Cu ₂ O (<i>Pn-3m</i>)	$a = b = c = 4.27 \text{ \AA}$	$a = b = c = 4.26 \text{ \AA}^b$
CeO ₂	$a = b = c = 5.46 \text{ \AA}$	$a = b = c = 5.41 \text{ \AA}^c$

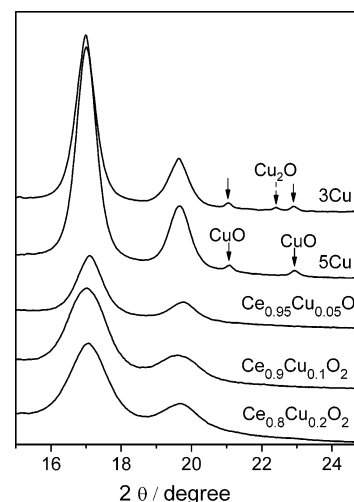
^a Ref 41a. ^b Ref 41b. ^c Ref 41c.**Figure 2.** Calculated crystal structure for CeO₂ and Ce_{0.75}Cu_{0.25}O₂ (the YZ plane is shown).

like the natural population analysis (NPA) or charges derived from fitting electrostatic potentials using grid-based methods (CHELPG).³⁹ In past articles, we have found the Mulliken population analysis useful for studying trends in charge redistribution within mixed-metal oxides.^{32,33}

Results and Discussion

A. Structural Properties. Figure 1 shows crystal structures for CuO, Cu₂O, and CeO₂. Bulk CuO adopts a monoclinic structure (*C2/c* space group) in which each Cu atom is bonded to *four* oxygen atoms. Bulk Cu₂O and CeO₂ have cubic structures in which the cations bond to *two* and *eight* oxygen neighbors, respectively. It is well-known that dopants can change the cell dimensions of the ceria lattice.^{16,18,33} In Table 1 are listed the calculated structural parameters for these oxides. They are in good agreement with experimental measurements.⁴⁰ DF calculations were performed for bulk Ce_{0.75}Cu_{0.25}O₂ and Ce_{0.875}Cu_{0.125}O₂. In Ce_{0.75}Cu_{0.25}O₂, there was a small tetragonal distortion in the unit cell ($a = b = 5.36 \text{ \AA}$, $c = 5.44 \text{ \AA}$), and the O atoms shifted with respect to their positions in pure ceria (see Figure 2). The Cu atoms essentially had four close oxygen neighbors (Cu–O bond distances of 1.92–1.95 Å), two oxygen neighbors at a medium distance (Cu–O bond distances of 2.31–2.33 Å), and two oxygen neighbors located too far away (Cu–O distance of 3.04–3.06 Å) for any effective bonding interaction. Due to their relatively small size with respect to Ce⁴⁺,⁴¹ the Cu cations do not fit well in the standard positions for the Ce cations in the ceria lattice and tend to adopt a nearly planar, four-coordinated first shell. Structural distortions have also been observed for Zr and Ca cations inside ceria,³³ producing strain into the oxide lattice and favoring the formation of O vacancies and reduction in H₂.^{16a} The introduction of O vacancies in the DF calculations for Ce_{0.75}Cu_{0.25}O₂ did not lift the atypical coordination of the Cu cations and led to small expansions (<0.05 Å) in the cell dimensions.

Figure 3 displays X-ray diffraction patterns collected at room temperature for a series of CuO_x/CeO₂ (top two traces) and Ce_{1-x}Cu_xO₂ samples (bottom three traces). Data were collected

**Figure 3.** XRD patterns for ceria impregnated with copper oxides (top two traces, 3% and 5% Cu by weight) and Ce_{1-x}Cu_xO₂ samples (bottom three traces).**TABLE 2: XRD Results for Ce_{1-x}Cu_xO₂ at Room Temperature^a**

oxide	lattice constant, a (Å)	O occupancy in lattice ^b	lattice strain
CeO ₂	5.400	1.00	0.85
Ce _{0.95} Cu _{0.05} O ₂	5.401	0.94	1.14
Ce _{0.9} Cu _{0.1} O ₂	5.401	0.88	1.24
Ce _{0.8} Cu _{0.2} O ₂	5.406	0.80	1.85

^a The estimated standard deviations are <0.01 Å for the lattice constant, <0.05 for the O occupancy, and <0.01 for the strain. (The derived χ^2 from least-squares analysis for the O occupancy is <0.01.) Uncertainties arising by the limitations of the refinement are of the order of ~0.05. ^b Without O vacancies, the value should be close to one.

in the 2θ range of 0–50°. Weak diffraction peaks for Cu₂O and/or CuO were detected for the CuO_x/CeO₂ systems. For the samples of Cu-doped ceria, which contained 1.9–8.1% Cu in weight, these peaks were not seen, and the diffraction pattern consisted only of the typical features for CeO₂,⁴² as expected for Ce_{1-x}Cu_xO₂ compounds.⁶ These features were broad due to the small size of the oxide particles (5–7 nm). Table 2 lists lattice constants, O occupancies, and strain parameters⁴³ determined in XRD studies for nanoparticles of CeO₂ and Ce_{1-x}Cu_xO₂. The small particle size of these systems puts a limit in the accuracy of our structural analysis,⁴³ and the “ a ” parameter listed in some cases may represent an average value for a pseudocubic phase with a slight tetragonal distortion. This will be further analyzed by using Raman spectroscopy. Each lattice parameter was calculated through a Rietveld refinement.⁴⁴ The results listed in Table 2 show very small variations in cell dimension as a consequence of doping ceria with Cu. In the theoretical studies described above, a small expansion was found for the cell volume of Ce_{1-x}Cu_xO₂ only after including O vacancies in the oxide lattice. Oxygen vacancies are present in the Ce_{1-x}Cu_xO₂ nanoparticles (see Table 2). The results of Rietveld refinement of the high- Q X-ray data indicate that Cu is substitutional in the ceria lattice and coexists with O vacancies (Ce⁴⁺ + O²⁻ → Cu²⁺ + O_{vacancy}). The amount of O vacancies and the magnitude of the strain in the oxide lattice both increase when the content of Cu is raised, as seen when ceria is doped with other metals.³² The results of the Rietveld refinement for the oxygens in Ce_{1-x}Cu_xO₂ than in pure CeO₂, and the Cu atoms in the mixed-metal oxides

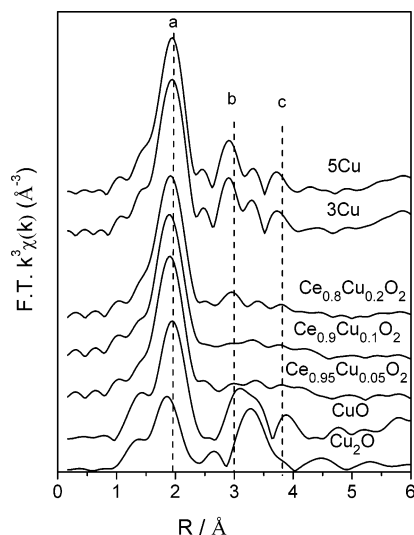


Figure 4. Cu K-edge k^2 -weighted Fourier transforms for the $\text{CuO}_x/\text{CeO}_2$ and $\text{Ce}_{1-x}\text{Cu}_x\text{O}_2$ samples, plus Cu_2O and CuO as standards.

are more disordered than the Ce atoms. This is consistent with the results of the DF calculations.

Cu K-edge XAFS spectra were collected for CuO (Cu^{2+} in a square planar symmetry), Cu_2O (Cu^+ coordinated by two oxygen atoms), pure metallic copper, and for the $\text{CuO}_x/\text{CeO}_2$ and $\text{Ce}_{1-x}\text{Cu}_x\text{O}_2$ samples. The corresponding Fourier transforms (FTs) of the EXAFS spectra (obtained by using the same k range: 2.5–11 \AA^{-1}) are presented in Figure 4. The line shape of the traces for the $\text{Ce}_{1-x}\text{Cu}_x\text{O}_2$ samples is very different from that found for CuO or $\text{CuO}_x/\text{CeO}_2$ samples, as expected because the Rietveld refinement of the X-ray data for $\text{Ce}_{1-x}\text{Cu}_x\text{O}_2$ demonstrates substitution of the Cu in the Ce positions of CeO_2 . A structural model in which there was a substitution of Ce by Cu in a rigid CeO_2 lattice did not fit well the FTs for the $\text{Ce}_{1-x}\text{Cu}_x\text{O}_2$ systems. The position of the main peak in the FTs points to a reorganization of the ceria oxygen lattice, such as seen in Figure 2, since a simple $\text{Cu} \leftrightarrow \text{Ce}$ substitution in a rigid oxide structure will give Cu–O and Cu–Ce distances equal to the cation–oxygen (2.34 \AA) and cation–cation (3.82 \AA) distances in CeO_2 . The results of the DF calculations for bulk $\text{Ce}_{0.75}\text{Cu}_{0.25}\text{O}_2$ and $\text{Ce}_{0.875}\text{Cu}_{0.125}\text{O}_2$ show a main set of Cu–O distances (1.92–1.95 \AA) that matches the bond length calculated for bulk CuO (1.94 \AA ; peak a, Figure 4). Additional Cu–O distances of ~ 2.3 (covered by peak a, Figure 4) and 3.05 \AA (peak b, Figure 4) were also found in the theoretical studies for bulk $\text{Ce}_{0.75}\text{Cu}_{0.25}\text{O}_2$ and $\text{Ce}_{0.875}\text{Cu}_{0.125}\text{O}_2$. Because of limitations in the FT range, peaks from 1.9 to 2.3 \AA cannot be resolved as separate features in an EXAFS scan. Fitting of the first shell in Figure 4 indicates that the amplitude for Cu–O in ceria is somewhat larger than that for pure CuO . According to the fitting, the Cu atoms in $\text{Ce}_{1-x}\text{Cu}_x\text{O}_2$ have coordination numbers (5–6) larger than that of CuO (4). The Cu–O peak at 3.05 \AA (peak b) and further coordination shells (Cu–Ce at ~ 3.8 \AA , peak c) are not clearly distinguishable in the corresponding FTs for $\text{Ce}_{1-x}\text{Cu}_x\text{O}_2$, implying that Cu introduces oxygen vacancies and a strong disorder into the oxide lattice. A comparison of the $\text{CuO}_x/\text{CeO}_2$ and $\text{Ce}_{1-x}\text{Cu}_x\text{O}_2$ FTs indicates that such a lack of medium-range order around the Cu cations is characteristic of the solid solutions and can be used as a fingerprint for the presence of Cu in a ceria lattice.

The XRD and XAFS results are well complemented by Raman results presented in Figure 5. The spectra show a main band at about 460 cm^{-1} that corresponds to the triply degenerate F_{2g} mode of fluorite CeO_2 (the only one allowed in first order).⁴⁵

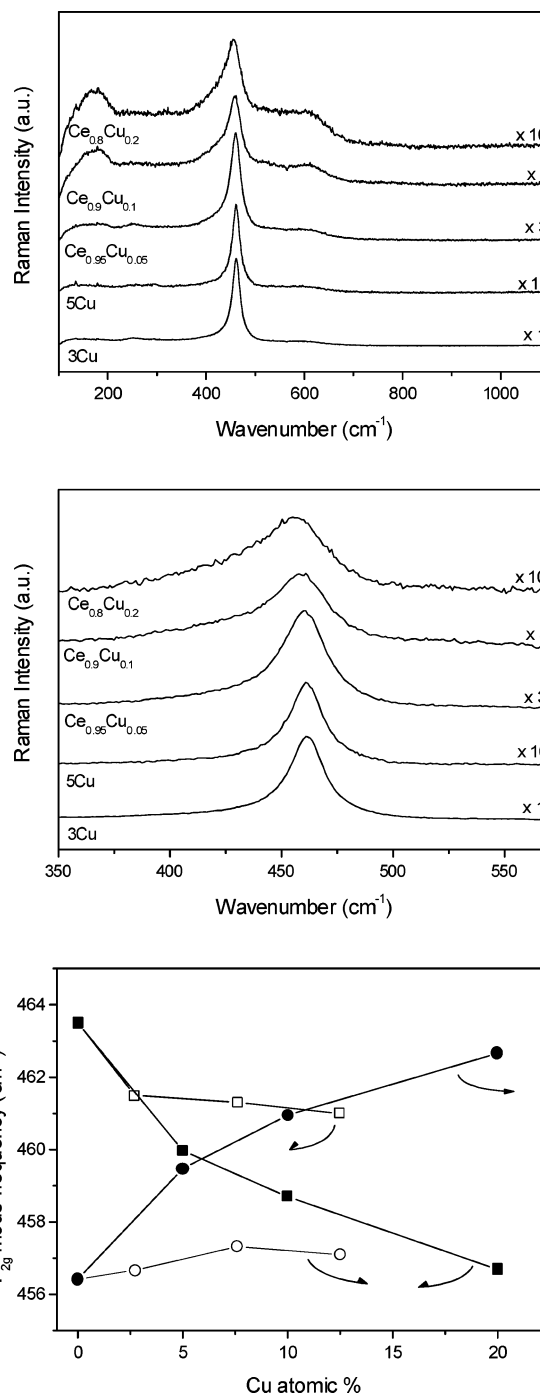


Figure 5. Top panel: Raman spectra for $\text{CuO}_x/\text{CeO}_2$ and $\text{Ce}_{1-x}\text{Cu}_x\text{O}_2$ samples. Center panel: Detail of the zone corresponding to the main F_{2g} mode band. Bottom panel: Frequency (squares) and width (circles) of the F_{2g} mode band for a series of samples prepared by impregnation ($\text{CuO}_x/\text{CeO}_2$, open symbols) and coprecipitation within microemulsions ($\text{Ce}_{1-x}\text{Cu}_x\text{O}_2$, full symbols). Fitting of the spectra to two bands was done to extract the values corresponding to only the F_{2g} mode band (see text).

A general decrease of the intensity is observed with increasing the copper content in any of the series. This can be related to an increased optical absorption with increasing the copper content, on the basis of UV–vis results observed for samples of this kind,^{7f} although other physical phenomena related to lattice disorder cannot be discarded.^{16a} Nevertheless, comparison of the two series of catalysts reveals that while the presence of copper only slightly affects the spectrum of pure CeO_2 in the catalysts prepared by impregnation (which has been related to

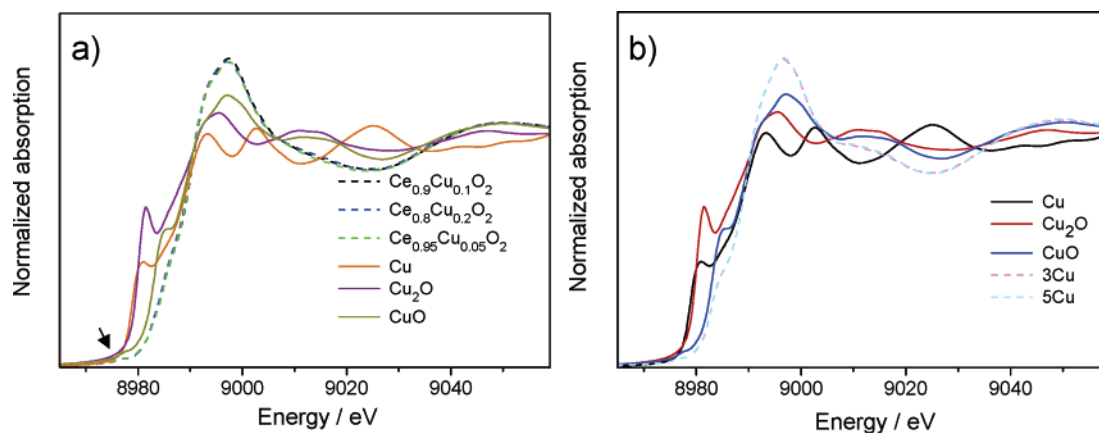


Figure 6. (a) Cu K-edge XANES spectra for CuO , Cu_2O , Cu , $\text{Ce}_{0.95}\text{Cu}_{0.05}\text{O}_2$, $\text{Ce}_{0.9}\text{Cu}_{0.1}\text{O}_2$, and $\text{Ce}_{0.8}\text{Cu}_{0.2}\text{O}_2$. (b) Cu K-edge XANES spectra for CuO , Cu_2O , Cu , and the CuO_x -impregnated samples (3% and 5% of Cu by weight).

TABLE 3: Calculated Mulliken Charges (*e*)

compound	$q(\text{Ce})$	$q(\text{Cu})$	$q(\text{O})$
CeO_2	1.42		−0.71
Cu_2O		0.35	−0.70
CuO		0.61	−0.61
$\text{Ce}_{0.875}\text{Cu}_{0.125}\text{O}_2$	1.41 to 1.44	0.82	−0.68 to −0.72
$\text{Ce}_{0.75}\text{Cu}_{0.25}\text{O}_2$	1.45 to 1.49	0.78	−0.67 to −0.73

a certain copper incorporation at surface or subsurface positions of the lattice, as detailed elsewhere),^{5a} it significantly affects the spectra of the $\text{Ce}_{1-x}\text{Cu}_x\text{O}_2$ series. First, a broad band extending between about 500 and 650 cm^{-1} , which has been related to the presence of oxygen vacancies,⁴⁶ shows increasing relative intensity with increasing the amount of copper, in agreement with XRD results that point to a decrease in the O occupancy (Table 2). Further evidence of copper incorporation in the lattice for the $\text{Ce}_{1-x}\text{Cu}_x\text{O}_2$ series is given by the shift and width observed in the main F_{2g} mode band, as shown in Figure 5. These observables certainly present influences of both phonon confinement and O vacancies, while inhomogeneous strain related to the presence of reduced states of cerium can also be involved.^{45a,46} However, the difference between the $\text{CuO}_x/\text{CeO}_2$ and $\text{Ce}_{1-x}\text{Cu}_x\text{O}_2$ samples is clearly visible at the bottom panel of Figure 5.

In addition to the F_{2g} -like contribution, a band centered at $\sim 175\text{ cm}^{-1}$ show also a relative growth with increasing the copper content in the $\text{Ce}_{1-x}\text{Cu}_x\text{O}_2$ series while the shape of the main band at $\sim 460\text{ cm}^{-1}$ suggests a concomitant relative growth of a new broad band centered at $\sim 425\text{ cm}^{-1}$. Note that this new band does not appear to be an effect of phonon confinement, known to produce a low-frequency tail in the main band, since such strong asymmetry would not be expected in that case.^{45a} Rather the bands at 175 and 425 cm^{-1} , which cannot be related to second-order bands,^{45b,47} can appear as a consequence of the mentioned tetragonal distortion, as proposed to occur also for Ce–Ca mixed oxide samples.¹⁸ Even though six active Raman modes would be expected in a pure tetragonal case, the presence of degenerated modes⁴⁸ or their overlapping with other bands can limit resolution in such case. Further details observed in the Raman spectra concern the presence of a weak band at 294 cm^{-1} in the spectrum of 5Cu, compatible with the presence of crystalline CuO in this sample.⁴⁹

B. Electronic Properties. Table 3 lists calculated Mulliken charges for CeO_2 , Cu_2O , CuO , and $\text{Ce}_{1-x}\text{Cu}_x\text{O}_2$ oxides. Cu is not a very electronegative element,⁴¹ and the calculated charge on the Cu cations of CuO and $\text{Ce}_{1-x}\text{Cu}_x\text{O}_2$ is substantially smaller than the formal value of “+2”. Our calculations and early works^{16,18} show that CeO_2 is not very ionic. Ceria is best

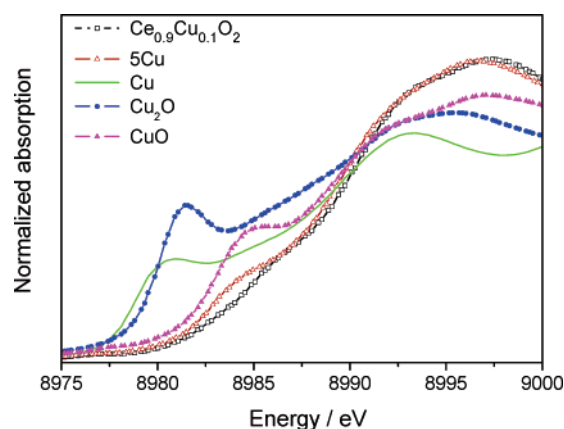


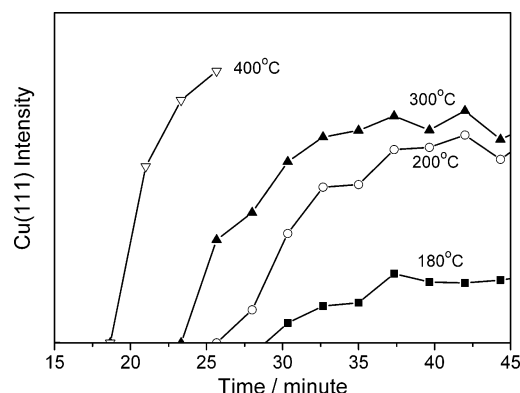
Figure 7. Cu K-edge spectra for a $\text{CuO}_x/\text{CeO}_2$ sample (5% of Cu by weight), $\text{Ce}_{0.9}\text{Cu}_{0.1}\text{O}_2$, and references of Cu , Cu_2O , and CuO .

described as an ionocovalent compound or covalent insulator.^{16,18} One important point in Table 3 is the significant difference observed between the charge distribution in $\text{Ce}_{0.75}\text{Cu}_{0.25}\text{O}_2$ and those in CuO or CeO_2 . For the Cu atoms, the positive charge in $\text{Ce}_{0.75}\text{Cu}_{0.25}\text{O}_2$ is larger than in CuO. This could be attributed to a certain increase in the number of O neighbors around the Cu cations (from 4 up to 6, according to the DFT and EXAFS results, see Figure 2). More difficult to explain is the increase of the positive charge on Ce when going from CeO_2 to $\text{Ce}_{0.75}\text{Cu}_{0.25}\text{O}_2$. This could be a consequence of a decrease in the Ce–O distance induced by the doping of Cu (see above).

Figures 6 and 7 compare Cu K-edge XANES spectra for CuO, Cu_2O , pure metallic copper, and the $\text{CuO}_x/\text{CeO}_2$ and $\text{Ce}_{1-x}\text{Cu}_x\text{O}_2$ samples. The spectral features provide important clues to differentiate the chemical state and local symmetry of the Cu species. A weak preedge peak (see arrow in Figure 6a) ascribed to a dipole-forbidden electronic transition of $1s \rightarrow 3d$ appears at 8977 eV for the Cu^{2+} species in CuO.⁴ This seems rather similar in the CuO and $\text{Ce}_{1-x}\text{Cu}_x\text{O}_2$ samples, indicating the similar local geometry already discussed by using EXAFS. In the 8978–8985 eV region of Figure 7, a dipole-allowed $1s \rightarrow 4p$ transition should take place and dominate the absorption spectrum,^{4,22,23} but there could be also a contribution from the Cu 3d levels to the final state due to Cu 4p–3d hybridization.⁴ The position of these transitions (determined from the first inflection point) is rather indicative of the local symmetry and oxidation state of Cu and has been summarized in Table 4. Typically, it shows increasing energies for an increasing Cu oxidation state and allows the differentiation of Cu^0 , Cu^+ , and

TABLE 4: Cu K-edge 1s \rightarrow 4p/3d Transition Energy^a

compound	energy (eV)
Cu	0.0
Cu ₂ O	0.9
CuO	4.4
5Cu	4.6
Ce _{0.95} Cu _{0.05} O ₂	5.6
Ce _{0.90} Cu _{0.10} O ₂	5.5
Ce _{0.80} Cu _{0.20} O ₂	5.5

^a The transition for a Cu foil is taken as the zero of the scale.**Figure 8.** Cu (111) peak intensity in the isothermal reduction of Ce_{0.8}Cu_{0.2}O₂ nanoparticles at different temperatures (5% H₂/He mixture, flow rate \sim 20 cc/min).

Cu²⁺ states, except in the case of tetracoordinated Cu⁺ compounds, which display energies similar to those of Cu²⁺ compounds.⁴ Further information may be obtained with the edge position, but the presence of the 1s \rightarrow 4p_{xy} transition(s) near or at the edge position, depending on local symmetry and chemical state, usually complicate the analysis.⁴ In addition, a comparison of edges with different shapes makes it difficult to perform a quantitative analysis of charge transfer.⁴ In any case, the results in Table 4 indicate that the Ce_{1-x}Cu_xO₂ samples have values of the 1s \rightarrow 4p/3d transitions \sim 1 eV above the characteristic position for CuO, while the CuO_x/CeO₂ samples have a rather similar energy value. Therefore, these XANES data imply that Cu in the doped ceria samples has an oxidation state higher than the cations in CuO or Cu₂O,⁵⁰ in agreement with the trend seen in Table 3 for calculated Mulliken charges. Furthermore, the relative intensity of the peaks at \sim 8998 eV in Figure 6a also indicates that Cu in Ce_{1-x}Cu_xO₂ has a higher positive charge than in CuO.⁵⁰ The experimental and theoretical results described in the last two sections illustrate the unique structural and electronic properties of the Cu atoms in Ce_{1-x}Cu_xO₂.

C. Chemical Reactivity: Reduction with H₂ and Reoxidation with O₂. The chemical reactivity of the doped Ce_{1-x}Cu_xO₂ samples was tested using reactions with H₂ and O₂ as probes. The isothermal reduction in 5% H₂/He and reoxidation in 5% O₂/He experiments were carried out with the doped samples. The results from the Ce_{0.8}Cu_{0.2}O₂ sample are used as an illustration in this work. Figure 8 presents the integrated Cu (111) peak intensities as a function of time for the reduction of Ce_{0.8}Cu_{0.2}O₂ in hydrogen at temperatures of 180, 200, 300, and 400 °C. The isothermal reduction experiments revealed the existence of an induction time, as was reported for the reduction of pure CuO.^{22,23} With a temperature increase, the induction time became shorter. A comparison with the results for CuO reduction in hydrogen under similar reaction conditions²² indicates that the reduction of the Cu in the doped ceria was slower. The copper atoms in Ce_{1-x}Cu_xO₂ were embedded in an oxide lattice that is not easy to reduce.^{16,18} In Figure 8, the

maximum intensity of the Cu (111) peak depends on the temperature of reduction, demonstrating that the Cu in the doped sample was only partially reduced to metallic Cu, especially at low temperatures. This observation is confirmed by the results of in-situ X-ray absorption spectroscopy, as will be shown below.

Figure 9 shows in-situ time-resolved X-ray diffraction patterns for the reduction (5% H₂/He) and reoxidation (5% O₂/He) of a Ce_{0.8}Cu_{0.2}O₂ sample at 300 °C. After the reduction process reached its maximum extent, based on the fact that the intensity of metallic Cu became constant, the gas was switched to 5% O₂/He from 5% H₂/He. The metallic Cu disappeared immediately right after the gas switch (this rapid transformation was observed even at a temperature as low as 180 °C). However, no CuO or Cu₂O crystalline phase was observed for the reoxidized sample, suggesting that the metallic copper segregated from the Ce_{0.8}Cu_{0.2}O₂ during the reduction process was mostly incorporated back into the ceria lattice during reoxidation. Similar XRD results were found for the reduction and reoxidation of Ce_{0.9}Cu_{0.1}O₂ and Ce_{0.95}Cu_{0.05}O₂.

Further evidence of the reversibility of this redox process is provided in Figure 10 which displays results for a Rietveld refinement of high-energy time-resolved XRD data ($Q = 0-15$ Å⁻¹) collected for the isothermal reduction and reoxidation of Ce_{0.8}Cu_{0.2}O₂ nanoparticles at 300 °C. During the reduction process, there is an increase in the cell parameter (top panel in Figure 10), probably as a consequence of the formation of some Ce³⁺ ions in the oxide lattice and/or hydrogen diffusion to the bulk.¹⁶ At the same time that pure Cu is formed, there is an increase of the O occupancy in the ceria lattice left behind by the metal (bottom panel in Figure 10). Under these conditions, pure ceria is very difficult to reduce³³ and contains a much smaller concentration of oxygen vacancies than Cu_{0.2}Ce_{0.8}O₂ (for example, see Table 2). Thus, the reduction process of the mixed oxide is complex, involving the removal of oxygen as gaseous H₂O and a reorganization of O atoms around the cerium cations. Once the Cu/Ce_{1-x}Cu_xO₂ system is reoxidized, the Cu moves back into the oxide matrix, and the concentration of O vacancies in ceria increases due to the stress introduced by the alien element.

In-situ time-resolved X-ray absorption spectra were also collected during the reduction and reoxidation of Ce_{1-x}Cu_xO₂. Figure 11 presents typical XANES spectra for the reduction in 5% H₂/He (Figure 11a) and reoxidation in 5% O₂/He (Figure 11b) of Cu_{0.2}Ce_{0.8}O₂ at 300 °C. The starting spectrum with the intense white line and no clear preedge gradually transformed into a spectrum with a sharp preedge and a less intense white line, similar to the spectrum for the metallic copper in Figures 6 and 7. The transformation is slow with respect to the reoxidation process (Figure 11b). The reoxidation of the formed metallic Cu was quick, confirming the observation from the time-resolved XRD results.

Cu K-edge EXAFS spectra were collected over the reduced and reoxidized samples after the samples were cooled to room temperature at the end of each process. The k^2 -weighted EXAFS spectra and corresponding Fourier transforms are shown in Figure 12, parts a and b, for the reduced sample with comparison to a standard of metallic copper. The EXAFS oscillations from the reduced sample showed basically the same trend as those for the metallic copper (Figure 12a). But the oscillation amplitude for the reduced sample was smaller (Figure 12a), indicating that metallic copper particles were formed from the reduction of Ce_{0.8}Cu_{0.2}O₂, as was also evident from the Cu-Cu peaks corresponding to the first to fourth metallic shells

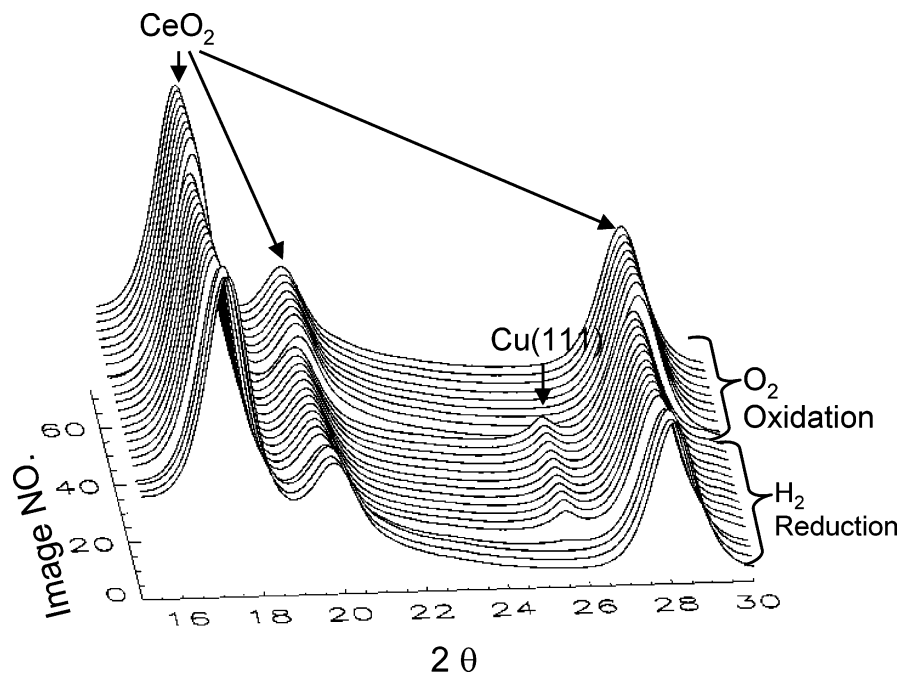


Figure 9. Time-resolved XRD patterns for the isothermal reduction and reoxidation of $\text{Ce}_{0.8}\text{Cu}_{0.2}\text{O}_2$ nanoparticles at 300 °C. (5% H_2/He mixture, flow rate ~ 20 cc/min; 5% O_2/He mixture, flow rate ~ 20 cc/min; $\lambda = 0.922$ Å).

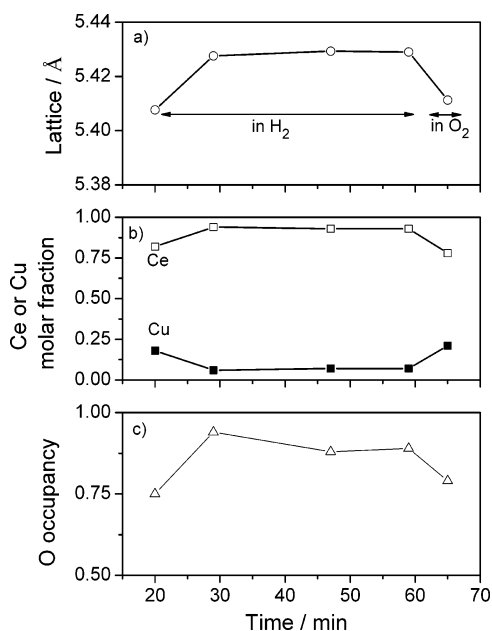


Figure 10. Rietveld refinements from high-energy time-resolved XRD data for the isothermal reduction and reoxidation of $\text{Ce}_{0.8}\text{Cu}_{0.2}\text{O}_2$ nanoparticles at 300 °C. (5% H_2/He mixture, flow rate ~ 20 cc/min; 5% O_2/He mixture, flow rate ~ 20 cc/min; $\lambda = 0.165$ Å). (a) Lattice parameters of the nanoparticles; (b) Cu and Ce molar fraction in the nanoparticles; (c) oxygen occupancy in the lattice of the nanoparticles.

(Figure 12b). XRD and EXAFS thus give evidence of the aggregation of Cu in parallel to the reduction step. A small peak appearing between 1.7 and 1.8 Å was observed in the time-resolved EXAFS of the reduced sample (Figure 12b), demonstrating that Cu in $\text{Ce}_{0.8}\text{Cu}_{0.2}\text{O}_2$ was not completely reduced at 300 °C. The distance of Cu–O was a bit less than those for the copper oxides references and the as-prepared $\text{Ce}_{1-x}\text{Cu}_x\text{O}_2$ samples, possibly because the O atoms were rearranged during the reduction process. Figure 12, parts c and d, present the k^2 -weight EXAFS spectra and corresponding Fourier transforms for the reoxidized sample with a comparison to the as-prepared

$\text{Ce}_{0.8}\text{Cu}_{0.2}\text{O}_2$. The oscillations for both samples were uniformly the same in the range shown in Figure 12c. The FT-EXAFS spectra (Figure 12d) again proved this observation with exactly the same Cu–O first shell; more importantly, the practical lack of order at medium range above the first shell is strongly indicative, as discussed in Figure 4, that Cu goes back to the initial position in the solid solution, that is, the one previous to the redox treatment. Nevertheless, certain changes around the Cu atoms might happen during the reoxidation, as indicated by the small changes in the relative intensity shells located above ~ 2 Å (Figure 12d). In this range, a precise structural analysis is difficult due to the noise in the raw data (Figure 12c). Thus, the results from in-situ X-ray absorption confirmed that the redox process was essentially reversible in the doped samples. The reversible nature of these processes demonstrates the special structural and chemical properties of the Cu-doped ceria materials. The special behavior of these materials plays an important role in the water-gas shift and CO oxidation reactions.⁵¹

Copper oxides are used as catalysts or catalyst precursors in many chemical reactions that involve hydrogen as a reactant or a product: methanol synthesis from CO ($\text{CO} + 2\text{H}_2 \rightarrow \text{CH}_3\text{OH}$) or CO_2 ($\text{CO}_2 + 3\text{H}_2 \rightarrow \text{CH}_3\text{OH} + \text{H}_2\text{O}$),⁵² the water-gas shift reaction ($\text{CO} + \text{H}_2\text{O} \rightarrow \text{CO}_2 + \text{H}_2$),^{7–9,53} methanol steam-reforming ($\text{CH}_3\text{OH} + \text{H}_2\text{O} \rightarrow \text{CO}_2 + 3\text{H}_2$),⁵⁴ oxidative methanol reforming ($\text{CH}_3\text{OH} + \frac{1}{4}\text{O}_2 + \frac{1}{2}\text{H}_2\text{O} \rightarrow \text{CO}_2 + \frac{5}{2}\text{H}_2$),⁵⁵ NO reduction ($\text{NO} + \text{H}_2 \rightarrow \frac{1}{2}\text{N}_2 + \text{H}_2\text{O}$),⁵⁶ and so forth. In general, the works reported in the literature do not agree in the mechanism proposed for the reduction of copper oxides. For example, experiments of H_2 temperature-programmed reduction show that the reduction of copper oxide dispersed on other oxides occurs in one, two, or even three steps.^{56–58} These discrepancies could be a consequence of the different conditions used in the reduction experiments, or they could originate from differences in the structural properties of the samples that contain the copper oxide. Our studies for the reaction of H_2 with CuO ^{22,23} and $\text{Ce}_{1-x}\text{Cu}_x\text{O}_2$ (this work) show substantial variations in the temperature of reduction and in the extent of the reduction

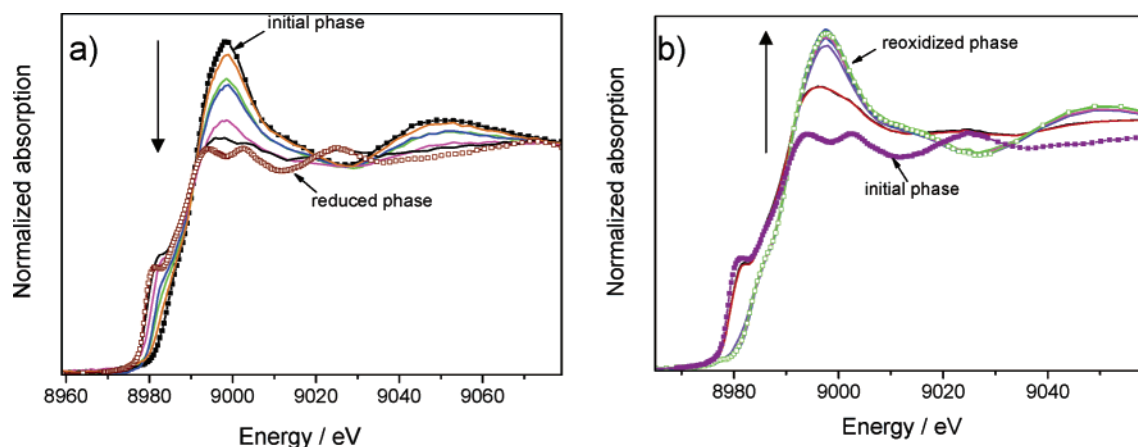


Figure 11. (a) Time-resolved Cu K-edge XANES spectra as a function of time at 300 °C during the reduction of $\text{Ce}_{0.8}\text{Cu}_{0.2}\text{O}_2$ in 5% H_2/He (flow rate ~ 20 cc/min). (b) Time-resolved Cu K-edge XANES spectra as a function of time at 300 °C during the reoxidation of the reduced sample in 5% O_2/He (flow rate ~ 20 cc/min).

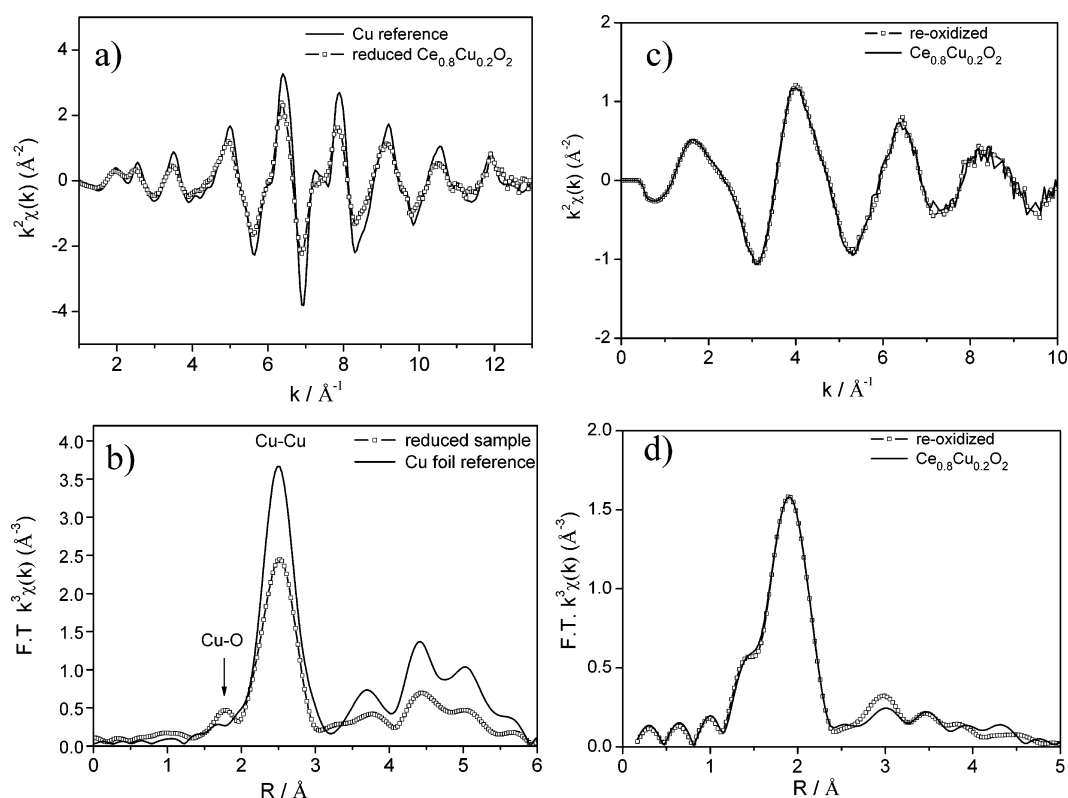


Figure 12. Panels (a) and (b): Cu K-edge k^2 -weighted EXAFS spectra for reduced $\text{Ce}_{0.8}\text{Cu}_{0.2}\text{O}_2$ (open square symbol in solid line) and a Cu foil reference (simple solid line) in k space and in R space, respectively. Panels (c) and (d): Cu K-edge EXAFS spectra for the reoxidized sample (open square symbol in solid line) and $\text{Ce}_{0.8}\text{Cu}_{0.2}\text{O}_2$ as prepared (simple solid line) in k space and in R space, respectively.

process, probably as a consequence of changes in the structural and electronic properties of the Cu cations.

Summary and Conclusions

The structural and electronic properties of $\text{Ce}_{1-x}\text{Cu}_x\text{O}_2$ nano systems prepared by a reverse microemulsion method were characterized with synchrotron-based X-ray diffraction, X-ray absorption spectroscopy, Raman spectroscopy, and density functional calculations. The Cu atoms embedded in ceria had an oxidation state higher than those of the cations in Cu_2O or CuO . The lattice of the $\text{Ce}_{1-x}\text{Cu}_x\text{O}_2$ systems still adopted a fluorite-type structure, but it was highly distorted with presence of local order defects and multiple cation–oxygen distances with respect to the single cation–oxygen bond distance seen in pure ceria. The doping of CeO_2 with copper introduced a large strain

into the oxide lattice and favored the formation of O vacancies. The chemical activities of the $\text{Ce}_{1-x}\text{Cu}_x\text{O}_2$ nanoparticles were tested using the reactions with H_2 and O_2 as probes. During the reduction in hydrogen, an induction time was observed and became shorter after raising the reaction temperature. The fraction of copper that could be reduced in the $\text{Ce}_{1-x}\text{Cu}_x\text{O}_2$ oxides also depended strongly on the reaction temperature. A comparison with data for the reduction of pure copper oxides indicated that the copper embedded in ceria was much more difficult to reduce. The reduction of $\text{Ce}_{1-x}\text{Cu}_x\text{O}_2$ was completely reversible without the generation of a significant amount of CuO or Cu_2O phases during reoxidation. This reversible process demonstrates the unusual structural and chemical properties of the Cu-doped ceria materials.

Acknowledgment. The research carried out at the Chemistry Department of Brookhaven National Laboratory was financed through Contract No. DE-AC02-98CH10086 with the U.S. Department of Energy, Division of Chemical Sciences. The NSLS is supported by the Divisions of Materials and Chemical Sciences of DOE. Work at the “Instituto de Catálisis (CSIC)” was done with financial support from CICYT (Contracts No. CTQ2004-03409/BQU and MAT2003-03925). Thanks are due to S.J. Khatib and M.A. Bañares for their help and facilities given to record Raman spectra, and to Z. Zhong for his help in the operation of beamline X17B1 of the NSLS.

References and Notes

- (1) Inoue, T.; Setoguchi, T.; Eguchi, K.; Arai, H. *Solid State Ionics* **1989**, *34*, 285.
- (2) (a) Park, S.; Vohs, J. M.; Gorte, R. J. *Nature* **2000**, *404*, 265. (b) Gorte, R. J.; Vohs, J. M.; McIntosh, S. *Solid State Ionics* **2004**, *175*, 1.
- (3) Lampe, U.; Gerblinger, J.; Meixner, H. *Sens. Actuators* **1992**, *B7*, 787.
- (4) (a) Kau, L.-S.; Solomon, D. J.; Penner-Hahn, J. E.; Hodgson, K. O.; Solomon, E. I. *J. Am. Chem. Soc.* **1987**, *109*, 6433. (b) Skårman, B.; Grandjean, D.; Benfield, R. E.; Hinz, A.; Andersson, A.; Wallenberg, L. R. *J. Catal.* **2002**, *211*, 119, and references therein.
- (5) (a) Martínez-Arias, A.; Hungria, A. B.; Fernández-García, M.; Conesa, J. C.; Munuera, G. *J. Phys. Chem. B* **2004**, *108*, 17983, and references therein. (b) Martínez-Arias, A.; Fernández-García, M.; Soria, J.; Conesa, J. C. *J. Catal.* **1999**, *182*, 367, and references therein. (c) Martínez-Arias, A.; Fernández-García, M.; Gálvez, O.; Coronado, J. M.; Anderson, J. A.; Conesa, J. C.; Soria, J.; Munuera, G. *J. Catal.* **2000**, *195*, 207.
- (6) Harrison, P. G.; Ball, I. K.; Azelee, W.; Daniell, W.; Goldfarb, D. *Chem. Mater.* **2000**, *12*, 3715.
- (7) (a) Liu, W.; Flytzani-Stephanopoulos, M. *J. Catal.* **1995**, *153*, 304. (b) Liu, W.; Flytzani-Stephanopoulos, M. *J. Catal.* **1995**, *153*, 317. (c) Li, Y.; Fu, Q.; Flytzani-Stephanopoulos, M. *Appl. Catal. B* **2000**, *27*, 179. (d) Qi, X.; Flytzani-Stephanopoulos, M. *Ind. Eng. Chem. Res.* **2004**, *43*, 3055. (e) Li, Y.; Fu, Q.; Flytzani-Stephanopoulos, M. *Catal. Today* **2004**, *93–95*, 241. (f) Shan, W.; Shen, W.; Li, C. *Chem. Mater.* **2003**, *15*, 4761.
- (8) Koryabkina, N. A.; Phatak, A. A.; Ruettinger, W. F.; Farrauto, R. J.; Ribeiro, F. H. *J. Catal.* **2003**, *217*, 233.
- (9) Jacobs, G.; Chenu, E.; Patterson, P. M.; Williams, L.; Sparks, D.; Thomas, G.; Davis, B. H. *Appl. Catal. A* **2004**, *258*, 203.
- (10) Zhu, T.; Kundakovic, L.; Dreher, A.; Flytzani-Stephanopoulos, M. *Catal. Today* **1999**, *50*, 381.
- (11) Shaw, E. A.; Rayment, T.; Walker, A. P.; Lambert, R. M.; Gauntlett, T.; Oldman, R. J.; Dent, A. *Catal. Today* **1991**, *9*, 197.
- (12) (a) Hoëvar, S.; Batista, J.; Levec, J. *J. Catal.* **1999**, *184*, 39. (b) Hoëvar, S.; Krasovec, U. O.; Orel, B.; Arico, A. S.; Kim, H. *Appl. Catal. B* **2000**, *28*, 113.
- (13) Liu, Y.; Hayakama, T.; Suzuki, K.; Hamakawa, S. *Catal. Commun.* **2001**, *2*, 195.
- (14) Men, Y.; Gnaser, H.; Zapf, R.; Hessel, V.; Ziegler, C.; Kolb, G. *Appl. Catal. A* **2004**, *277*, 83.
- (15) Papavasiliou, J.; Avgouropoulos, G.; Ioannides, T. *Catal. Commun.* **2004**, *5*, 231.
- (16) (a) Wang, X.; Hanson, J. C.; Liu, G.; Rodriguez, J. A.; Iglesias-Juez, A.; Fernández-García, M. *J. Chem. Phys.* **2004**, *121*, 5434. (b) Wang, X.; Hanson, J. C.; Rodriguez, J. A.; Belver, C.; Fernández-García, M. *J. Chem. Phys.* **2005**, *122*, 154711.
- (17) (a) Fernández-García, M.; Martínez-Arias, A.; Guerrero-Ruiz, A.; Conesa, J. C.; Soria, J. *J. Catal.* **2002**, *211*, 326. (b) Iglesias-Juez, A.; Hungria, A. B.; Gálvez, O.; Martínez-Arias, A.; Fernández-García, M.; Conesa, J. C.; Soria, J. *Stud. Surf. Sci. Catal.* **2001**, *138*, 347. (c) Fernández-García, M.; Martínez-Arias, A.; Hungria, A. B.; Iglesias-Juez, A.; Conesa, J. C.; Soria, J. *Phys. Chem. Chem. Phys.* **2002**, *4*, 2473. (d) Hungria, A. B.; Martínez-Arias, A.; Fernández-García, M.; Iglesias-Juez, A.; Guerrero-Ruiz, A.; Calvino, J. J.; Conesa, J. C.; Soria, J. *Chem. Mater.* **2003**, *15*, 4309.
- (18) Rodriguez, J. A.; Wang, X.; Hanson, J. C.; Liu, G.; Iglesias-Juez, A.; Fernández-García, M. *J. Chem. Phys.* **2003**, *119*, 5659.
- (19) Fu, Q.; Weber, A.; Flytzani-Stephanopoulos, M. *Catal. Lett.* **2001**, *77* (1–3), 87.
- (20) Bunluesin, T.; Gorte, R.; Graham, G. *Appl. Catal. B* **1998**, *15*, 107.
- (21) Hilaire, S.; Wang, X.; Luo, T.; Gorte, R. J.; Wagner, J. *Appl. Catal. A* **2001**, *215*, 271.
- (22) (a) Kim, J.-Y.; Rodriguez, J. A.; Hanson, J. C.; Frenkel, A. I.; Lee, P. L. *J. Am. Chem. Soc.* **2003**, *125*, 10684. (b) Rodriguez, J. A.; Kim, J. Y.; Hanson, J. C.; Perez, M.; Frenkel, A. I. *Catal. Lett.* **2003**, *85*, 247.
- (23) Wang, X. Q.; Hanson, J. C.; Frenkel, A. I.; Kim, J.-Y.; Rodriguez, J. A. *J. Phys. Chem. B* **2004**, *108*, 13667.
- (24) Chupas, P. J.; Ciruolo, M. F.; Hanson, J. C.; Grey, C. P. *J. Am. Chem. Soc.* **2001**, *123*, 1694.
- (25) Hammersely, A. P.; Svensson, S. O.; Thompson, A. *Nucl. Instrum. Methods Phys. Res.* **1994**, *346*, 321.
- (26) Lytle, F.; Sayers, D.; Stern, E. The History and Modern Practice of EXAFS Spectroscopy. In *Advances in X-ray Spectroscopy*; Bonnelle and Mande, Eds.; Pergamon Press: Elmsford, NY, 1982.
- (27) Bera, P.; Priolkar, K. R.; Sarode, P. R.; Hegde, M. S.; Emura, S.; Kumashiro, R.; Lalla, N. P. *Chem. Mater.* **2002**, *14*, 3591.
- (28) Newville, M.; Ravel, B.; Haskel, D.; Rehr, J. J.; Stern, E. A.; Yacoby, Y. *Physica B* **1995**, *208–209*, 154.
- (29) Sayers, D. E.; Bunker, B. A. In *X-ray Absorption: Principles, Applications, Techniques of EXAFS, SEXAFS, and XANES*; Koningsberger, D. C., Prins, R., Eds.; John Wiley & Sons: New York, 1988; p 211.
- (30) (a) Milman, V.; Winkler, B.; White, J. A.; Pickard, C. J.; Payne, M. C.; Akhmatkaya, E. V.; Nobes, R. H. *Int. J. Quantum Chem.* **2000**, *77*, 895. (b) Payne, M. C.; Allan, D. C.; Arias, T. A.; Johannopoulos, J. D. *Rev. Mod. Phys.* **1992**, *64*, 1045.
- (31) Liu, G.; Rodriguez, J. A.; Hrbeek, J.; Dvorak, J.; Peden, C. H. F. *J. Phys. Chem. B* **2001**, *105*, 7762.
- (32) (a) Rodriguez, J. A.; Etcheberria, A.; González, L.; Maiti, A. *J. Chem. Phys.* **2002**, *117*, 2699. (b) Rodriguez, J. A.; Azad, S.; Wang, L.-Q.; García, J.; Etcheberria, A.; González, L. *J. Chem. Phys.* **2003**, *118*, 6562.
- (33) Rodriguez, J. A.; Hanson, J. C.; Kim, J.-Y.; Liu, G.; Iglesias-Juez, A.; Fernandez-Garcia, M. *J. Phys. Chem. B* **2003**, *107*, 3535.
- (34) (a) Dawson, I.; Bristowe, P. D.; Lee, M. H.; Payne, M. C.; Segall, M. D.; White, J. M. *Phys. Rev. B* **1996**, *54*, 13727. (b) Lindan, P. J. D.; Harrison, N. M.; Holender, J. M.; Gillan, M. J. *Chem. Phys. Lett.* **1996**, *261*, 246.
- (35) Vanderbilt, D. *Phys. Rev. B* **1990**, *41*, 7892.
- (36) Monkhorst, H. J.; Pack, J. D. *Phys. Rev. B* **1976**, *13*, 5188.
- (37) Perdew, J. P.; Burke, K.; Ernzerhof, M. *Phys. Rev. Lett.* **1996**, *77*, 3865.
- (38) (a) Segall, M. D.; Pickard, C. J.; Shah, R.; Payne, M. C. *Phys. Rev. B* **1996**, *54*, 16317. (b) Sánchez-Portal, D.; Artacho, E.; Soler, J. M. *J. Phys.: Condens. Matter* **1996**, *8*, 3859.
- (39) Wiber, K. B.; Rablen, P. R. *J. Comput. Chem.* **1993**, *14*, 1504, and references therein.
- (40) (a) PDF #33-0480, JCPDS Powder Diffraction File, Int. Center for Diffraction Data Swarthmore, PA, 1989. (b) Milman, V.; Winkler, B.; White, J. A.; Pickard, C. J.; Payne, M. C.; Akhmatkaya, E. V.; Nobes, R. H. *Int. J. Quantum Chem.* **2000**, *77*, 895.
- (41) (a) Shannon, R. D. *Acta Crystallogr.* **1976**, *A32*, 751. (b) Shannon, R. D.; Prewitt, C. T. *Acta Crystallogr.* **1969**, *B25*, 925. (c) Shannon, R. D.; Prewitt, C. T. *Acta Crystallogr.* **1970**, *B26*, 1046.
- (42) (a) Zhang, F.; Jin, Q.; Chan, S.-W. *J. Appl. Phys.* **2004**, *95*, 4319. (b) PDF #34-0394, JCPDS Powder Diffraction File, Int. Center for Diffraction Data, Swarthmore, PA, 1993.
- (43) Fernandez-Garcia, M.; Martínez-Arias, A.; Hanson, J. C.; Rodriguez, J. A. *Chem. Rev.* **2004**, *104*, 4063.
- (44) (a) Larson, A. C.; von Dreele, R. B. *GSAS General Structure Analysis System*. Report LAUR 86-748; Los Alamos National Laboratory: Los Alamos, NM, 1995. (b) Rietveld, A. M. *J. Appl. Cryst.* **1969**, *2*, 65. (c) Toby, B. H. *J. Appl. Crystallogr.* **2001**, *34*, 210.
- (45) (a) Spanier, J. E.; Robinson, R. D.; Zhang, F.; Chan, S.-W.; Herman, I. P. *Phys. Rev. B* **2001**, *64*, 245407. (b) Weber, W. H.; Hass, K. C.; McBride, J. R. *Phys. Rev. B* **1993**, *48*, 178.
- (46) McBride, J. R.; Hass, K. C.; Poindexter, B. D.; Weber, W. H. *J. Appl. Phys.* **1994**, *76*, 2435.
- (47) Nakajima, A.; Yoshihara, A.; Ishigame, M. *Phys. Rev. B* **1994**, *50* (13), 297.
- (48) Yashima, M.; Arashi, H.; Kakihana, M.; Yoshimura, M. *J. Am. Ceram. Soc.* **1994**, *77*, 1067.
- (49) Xu, J. F.; Ji, W.; Shen, Z. X.; Li, W. S.; Tang, S. H.; Ye, X. R.; Jia, D. Z.; Xin, X. Q. *J. Raman Spectrosc.* **1994**, *30*, 413.
- (50) Jeon, Y.; Lu, F.; Jhans, H.; Shaheen, S. A.; Liang, G.; Croft, M.; Ansari, P. H.; Ramanujachary, K. V.; Hayri, E. A.; Fine, S. M.; Li, S.; Feng, X. H.; Greenblatt, M.; Greene, L. H.; Tarascon, J. M. *Phys. Rev. B* **1987**, *36* (7), 3891.
- (51) Wang, X.; Rodriguez, J. A.; Hanson, J. C.; Gamarrá, D.; Martínez-Arias, A.; Fernández-García, M. In preparation.
- (52) (a) Klier, K. *Adv. Catal.* **1982**, *31*, 243. (b) Li, J. L. Takeguchi, T.; Inui, T. *Appl. Catal. A* **1996**, *139*, 97.
- (53) Newsome, D. S. *Catal. Rev.—Sci. Eng.* **1980**, *21*, 275.
- (54) Peppley, B. A.; Amphlett, J. C.; Kearns, L. M.; Mann, R. F. *Appl. Catal. A* **1999**, *179*, 31.
- (55) Reitz, T. L.; Lee, P. L.; Czaplewski, K. F.; Lang, J. C.; Popp, K. E.; Kung, H. T. *J. Catal.* **2001**, *199*, 193.
- (56) Dow, W.-P.; Huang, T.-J. *Appl. Catal. A* **1996**, *141*, 17.
- (57) Dow, W.-P.; Wang, Y.-P.; Huang, T. J. *J. Catal.* **1996**, *160*, 155.
- (58) Fernández-García, M.; Rodríguez-Ramos, I.; Ferreira-Aparicio, P.; Guerrero-Ruiz, A. *J. Catal.* **1998**, *178*, 253.